Virus-Directed Design of a Flexible $BaTiO_3$ Nanogenerator

Chang Kyu Jeong,[†,§] Insu Kim,[†,§] Kwi-Il Park,[†] Mi Hwa Oh,[‡] Haemin Paik,[†,⊥] Geon-Tae Hwang,[†] Kwangsoo No,[†] Yoon Sung Nam,[†,‡,*] and Keon Jae Lee[†,*]

[†]Department of Materials Science and Engineering, and [‡]Department of Biological Sciences, Korea Advanced Institute of Science and Technology (KAIST), 291 Daehak-ro, Yuseong-gu, Daejeon 305-701, Republic of Korea. [§]These authors contributed equally to this work. [⊥]Present address: Department of Materials Science, California Institute of Technology, Pasadena, California 91125, United States.

ABSTRACT Biotemplated synthesis of functional nanomaterials has received increasing attention for applications in energy, catalysis, bioimaging, and other technologies. This approach is justified by the unique abilities of biological systems to guide sophisticated assembly and organization of molecules and materials into distinctive nanoscale morphologies that exhibit physicochemical properties highly desirable for specific purposes. Here, we present a high-performance, flexible nanogenerator using anisotropic $BaTiO_3$ (BTO) nanocrystals synthesized on an M13 viral template through the genetically programmed self-assembly of metal ion precursors. The filamentous viral template realizes the formation of a highly entangled, well-dispersed network of anisotropic BTO nanostructures with high crystallinity and piezoelectricity. Even without the use of additional structural stabilizers, our virus-enabled flexible nanogenerator exhibits a high electrical output up to ~300 nA and ~6 V, indicating the importance of nanoscale structures for device performances. This study shows the biotemplating approach as a facile method to design and fabricate nanoscale materials particularly suitable for flexible energy harvesting applications.

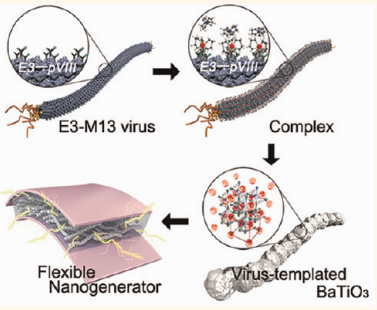

KEYWORDS: M13 bacteriophage · biosynthesis · virus template · barium titanate ($BaTiO_3$) · piezoelectric · nanogenerator

Energy harvesting from renewable resources became a critical issue in our civilization because of environmental problems associated with fossil fuel-based energy technologies.[1] In particular, mechanical resources are very common and easily accessible in our everyday lives, making them distinctive from other renewable energy sources (*e.g.*, solar, geothermal, and biomass energies).[2,3] While several methods have been developed to convert mechanical energy into electricity,[4] piezoelectric systems have attracted increasing attention due to the direct conversion from mechanical energy to electricity.[3,5,6] A nanogenerator, which is a piezoelectric material-based energy-harvesting device,[7−12] has been studied using perovskite-structured ceramics, such as $PbZr_xTi_{1-x}O_3$ (PZT)[13−15] and $BaTiO_3$ (BTO).[3,16] BTO is a particularly attractive material due to its lead-free biocompatibility with high piezoelectricity.[17] However, typical methods to synthesize perovskite nanomaterials use toxic organic solvents and alkoxide precursors.[18,19] Furthermore, the surface of resultant nanomaterials is often contaminated by polymeric residues and surfactants, which can cause detrimental effects to the original properties of materials.[20]

Recently, as an alternative to conventional techniques, a new synthetic approach based on biological templates has gained popularity to generate new inorganic architectures with unique properties under ambient conditions.[21,22] For instance, DNA,[23] virus,[24,25] and microorganisms[26] have been explored as a template to control the materials properties (*e.g.*, composition, crystallinity, phase, morphology, *etc.*) as well as develop environmentally benign and energy-efficient fabrication processes (*e.g.*, biomineralization).[27,28] The biogenic routes to the fabrication of functional nanomaterials have been investigated for a wide range of applications, including energy storage,[29,30] photovoltaics,[31] water oxidation,[32,33] magnetic resonance imaging,[34] *etc.*[35,36] In particular, viruses have been successfully utilized as a genetically programmable toolkit for the self-assembly of nanoarchitectured inorganic structures through specific peptide-mediated interactions.[37] For instance, a filamentous M13

* Address correspondence to yoonsung@kaist.ac.kr, keonlee@kaist.ac.kr.

Received for review September 5, 2013 and accepted November 14, 2013.

Published online November 14, 2013
10.1021/nn404659d

virus encapsulates a single-stranded DNA with 2700 copies of pVIII major coat proteins along the longitudinal viral axis. The genetic modification of pVIII to render an affinity toward various inorganic materials allows the formation of anisotropic nanomaterials through biotemplated synthesis in an aqueous solution under mild conditions. This noteworthy biological scaffold has been investigated to realize various energy devices (*e.g.*, battery and solar cells) with outstanding performances because the filamentous shape of an M13 virus can generate a percolated network for well-dispersed nanostructures.[29−31,38] Likewise, in nanostructure-embedded piezoelectric devices, the homogeneous dispersion of piezoelectric nanomaterials has been regarded as a key issue for high electrical outputs as demonstrated in our recent works. For example, Park *et al.* used graphitic carbon nanomaterials as a dispersant for nanogenerators.[3,15] On the contrary, we emphasize that a percolated network of piezoelectric nanomaterials dispersed in a flexible elastomer matrix can be generated without toxic dispersion enhancers by employing a simple M13-based biosynthesis for effective energy harvesting, which enables one to power the micro/nanoelectronic devices for indoor and *in vivo* environments. Recently, it was reported that the piezoelectric properties of the M13 virus can be utilized to generate electrical energy,[39] although the energy level from the virus was significantly lower than that from inorganic-based energy harvesters.[3,13,15,40]

In this work, we propose a high-performance, flexible nanogenerator device based on the stable network of anisotropic BTO nanostructures prepared using an M13 virus as a template. An M13 virus was genetically engineered to display a glutamate trimer (EEE or E3) at the N-terminus of each pVIII protein. The virus is denoted as 'E3-M13'. The same virus was previously utilized for the biomineralization of amorphous iron phosphate (a-$FePO_4$).[29] In this work, it was found that barium and titanium precursor ions were also strongly associated with the E3 peptide *via* metal ion−peptide coordination. The prepared virus-metal ionic complexes were used to synthesize virus-templated BTO nanostructures. The filamentous shape of M13 can guide the formation of a uniform dispersion of anisotropic piezoelectric materials, which is vitally important to generate effective and well-distributed piezopotential. The interaction of the metal ions with the viral capsid proteins, forming virus-metal ionic complexes, and the subsequent formation of anisotropic BTO nanocrystal structures were carefully characterized. The virus-templated BTO nanostructures with high crystallinity and effective piezoelectricity were incorporated into an elastomeric matrix to fabricate a virus-templated flexible piezoelectric nanogenerator.

RESULTS AND DISCUSSION

The overall synthesis processes of virus-templated BTO nanostructures are presented in Figure 1a. The genetically modified M13 virus was incubated in ligand solutions to form a virus-metal ionic complex, achieving highly percolated and well-dispersed nanostructures obtained *via* calcination. The simulation for piezoelectric potential with a simplified virus-templated BTO model in an elastomer matrix indicates that the entangled network structure of the anisotropic virus-templated BTO nanostructures is crucial to the energy harvesting performances of a nanogenerator (Figure 1b). The piezopotential distribution of anisotropic BTO nanostructures is presented by a color code with the x-axial tensile stress. With this finite element analysis (FEA), the virus-templated filamentous BTO nanostructure can effectively generate electrical energy from mechanical agitation much more effectively than BTO nanoparticles (NPs), which show poor dispersion stability (see Supporting Information).

Figure 1c−e describes the detailed synthetic procedures of virus-templated BTO nanostructures. The pVIII major coat proteins can strongly interact with positively charged metal ion precursors because of the genetically incorporated extra carboxylates, as illustrated in Figure 1c. To prepare a virus-metal ionic complex (Figure 1d), a 200 mM barium glycolate solution was initially incubated with 10^{13} pfu·mL^{-1} E3-M13 for 2 h at ambient temperature, and then 200 mM titanium glycolate was added to the virus solution. The titanium precursor solution was added at 80 °C and pH ≥10 for condensation and diffusion of the two glycolate precursors onto the viral surface. The sequential addition is very important because titanium glycolate chelate, $[Ti^{IV}(OCH_2CH_2O)_3]^{2-}$, is negatively charged and thus can be electrostatically repulsed by highly negative charged E3-M13. In contrast, barium glycolate chelate, $[Ba^{II}(HOCH_2CH_2OH)_4(OH_2)]^{2+}$, is positively charged,[41] so this barium precursor can be easily attracted by the virus. Sequentially, the barium glycolate complexed with the virus can draw the titanium glycolate through electrostatic attraction and hydrogen bonding.[41,42] It is well-known that octahedral titanium glycolate and the nine-coordinated barium glycolate can be linked by hydrogen-bonded pairs.[41] If these two precursors were added together at the same time, the titanium glycolate would be rapidly self-polymerized in an aqueous solution, generating large precipitated aggregates, while the barium glycolate would exist as a dissolved ligand. In our biotemplate approach for a BTO-based nanogenerator, the heat treatment is needed to form a perovskite crystalline structure due to the high crystallization energy of BTO.[43] Although the virus-template was eliminated during calcination, the anisotropic filamentous shape for BTO nanostructure was well maintained with high crystallinity (Figure 1e). As we expected, the calcined species using the single-step incubation process were only titanium-rich materials, such as $BaTi_4O_9$ and $BaTi_2O_5$ (Figure S2).

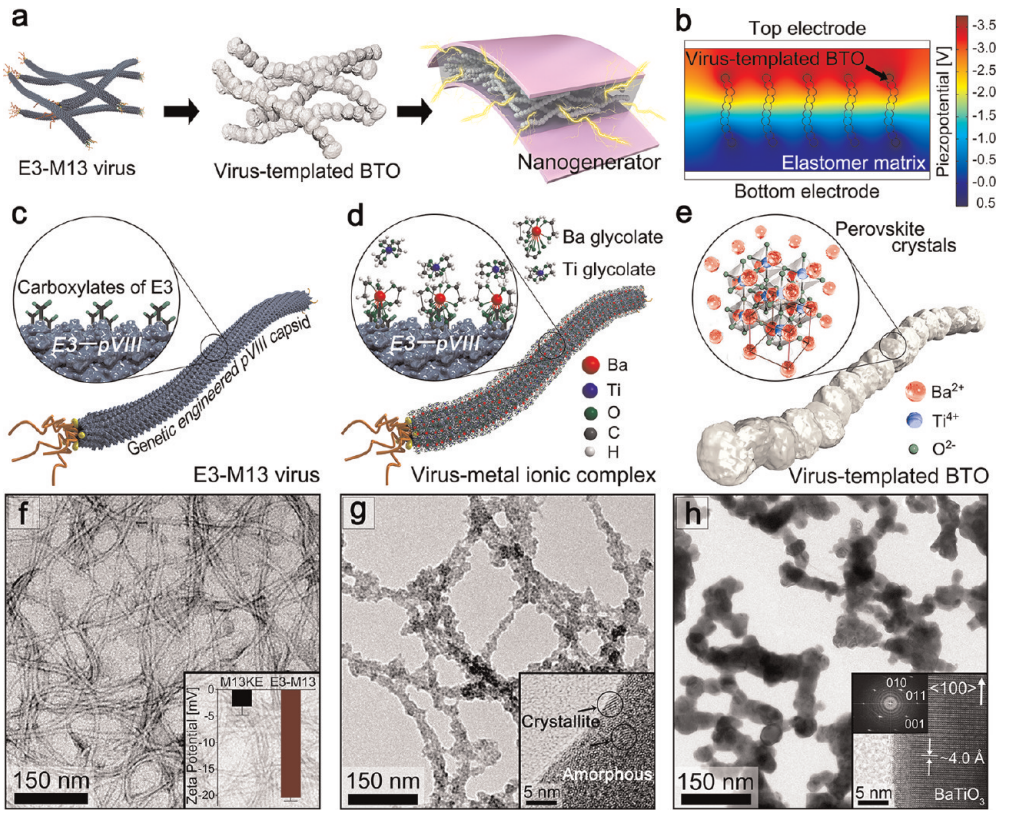

Figure 1. Schematic diagram and TEM images of virus-templated BTO synthesis for nanogenerator. (a) Overall fabrication process of a virus-templated BTO based piezoelectric nanogenerator. (b) Simulation for the piezoelectric potential of dispersed virus-shaped BTO in a matrix (mechanical tensile stress of 0.33%). (c−e) Schemes of each step to explain synthetic processes. (c) M13 bacteriophage is shown with the major capsid proteins (pVIII) genetically engineered. Three glutamates (E3) are expressed on the N-terminus of pVIII. (d) Virus-metal ion complexation occurs when barium/titanium glycolates interact with the E3 modified coat proteins. (e) Virus-templated BTO is formed by calcination for not only crystallization but also elimination of phage templates. BTO crystals have a perovskite structure that can show excellent piezoelectricity. (f−h) TEM micrographs of each step in the virus-templated BTO synthesis. (f) The well-entangled E3-M13 viruses negative stained. (Inset) Zeta-potential analysis showing that the E3-M13 virus has more net negative charges than the wild-type virus (M13KE). (g) Morphology of the virus-metal ion complex with glycolate precursors. (Inset) The HRTEM image presents that the complex materials are composed of an amorphous matrix of oxides/glycolates and some titanium oxide crystallites. (h) Virus-templated BTO nanocrystals after calcination. (Inset) The crystal fringe image by HRTEM corresponding to the lattice parameter of BTO perovskite structure ($a = b = 3.994$ Å, $c = 4.038$ Å). The power spectrum from the fast-Fourier transform verifies the rectangular patterns, exhibiting the tetragonal phase of the synthesized BTO.

The overall morphologies and properties of the produced materials during the virus-templated synthesis were analyzed, as shown in Figure 1f−h. Figure 1f is a transmission electron microscope (TEM) image of E3-M13 virus negatively stained capsids by uranyl acetate, which shows a well-entangled filamentous structure having a diameter of about 7 nm. The zeta-potential analysis of both E3-M13 and wild-type M13 (M13KE) in tris buffered saline (TBS) at pH 10 confirms that the E3-M13 is more negatively charged than M13KE (inset of Figure 1f). After the incubation of glycolates for the assembly of metal ligands onto the viral surface, the width of the resulting structure increased to about 20−30 nm, while the percolated structure of viruses was well maintained (Figure 1g). Some crystallites in an amorphous matrix of the virus-metal ionic complex were observed presumably due to the hydrolysis of titanium glycolates, as presented by high resolution TEM (HRTEM) analysis (inset of Figure 1g). These crystallites seem to be tiny TiO_2 domains as determined by selected-area electron diffraction (SAED) rings; however, the entire X-ray diffraction (XRD) patterns of this virus-templated intermediate show no peak because most of the complex consists of glycolates/metal oxides-based amorphous regions (Figure S3). After calcination, the final virus-templated BTO nanostructures with the well-dispersed morphology and anisotropic shape were 50−100 nm in width as a result of the heat treatment (Figure 1h and Figure S5). This grain size of nanocrystals was large enough to form the tetragonal phase, which is essential for piezoelectric properties.[44] HRTEM and rectangular patterns in the power spectrum of virus-templated BTO nanostructures (insets of Figure 1h) show the formation of the tetragonal perovskite structure of BTO from the virus-templated complex. A comparison of syntheses without the viral template and with wild-type M13KE is also described in Supporting Information.

The M13 virus expressing trimeric or tetrameric glutamates have been proved to be highly useful for the templated synthesis of metal oxides; however, the chemical nature of the virus-metal ionic complexes has not been well examined. The regions of negatively charged amino acid lumps on a viral surface have been just regarded as an origin of Coulombic attractive force with metal cations. Moreover, our experiment and some previously reported methods have used chelates or nonpristine ions as precursors, rather than just using purely aqueous metal cations. To investigate the chemical properties of virus-templated materials, we carried out attenuated total reflection infrared (ATR-IR) spectroscopy and X-ray photoelectron spectroscopy (XPS). In the ATR-IR spectra of the virus-metal ionic complex (Figure 2a—i), the two humps near 2987 and 2901 cm^{-1} are attributed to the alkanes in the bound glycolates. The bands at 1395 and 1066 cm^{-1} are assigned to the hydroxyl groups and C—O bonds in EG-based precursors, respectively. In addition, there is only a carboxylic C—O bond at 1252 cm^{-1} without a C═O bond. These results indicate that both of the two oxygen atoms in the carboxylic group of glutamate are involved in the chelation of the metal-center, as in the similar manner with the EG ligand. The strong chelating capability of glutamate is reasonable since the electron density of carboxylate is higher than that of the hydroxyl group in EG. The metal—oxygen coordinating bond of chelates is visible as a multitude of peaks[45] below 670 cm^{-1}. The small band at 860 cm^{-1} corresponding to the Ti—O stretching vibrations is observed[46] in not only as-calcined final virus-templated BTO but also the virus-metal ionic complex. Since the chelation of our approach is achieved by oxygen atoms surrounding a metal element, the O1s XPS analysis is vital to inspect the chemical state and binding configuration of the complex (Figure 2b—i). In the broad spectra, the oxygen—metal chelating bond can be detected at a lower binding energy (530.8 eV) than C—O binding energy (531.9 eV).[47] Moreover, there is an obvious envelope of metal oxide at the lowest energy (529.5 eV), which accords with the crystalline and amorphous TiO_2 observed in the results of HRTEM and SAED from the virus-metal ionic complex. The shallow shoulder at 533.6 eV corresponds to physically adsorbed water molecules on organic elements.[48] The XPS curve of pure virus shows no metal-related envelope (Figure S8); that is, the complexation and chelation events between the virus scaffold and precursors definitely may happen during the incubation process. On the other hand, the deep and wide trenches below 600 cm^{-1} in the IR spectra (out of window) are characteristic to BTO as reported previously (Figure 2a-ii).[46] Some deviated signals of the IR analysis of BTO are induced by oxidized hydrocarbons. Figure 2b-ii only shows that the BTO specific XPS peak exists at 528.9 eV after calcination. The down-shift of the oxide peak compared to the virus-metal ion complex results from the elimination of organic residues. A good agreement between the theoretical value and measurement of the O1s peak from BTO is observed despite the inevitable contamination with carbonaceous species from equipment (530.7 eV).[49]

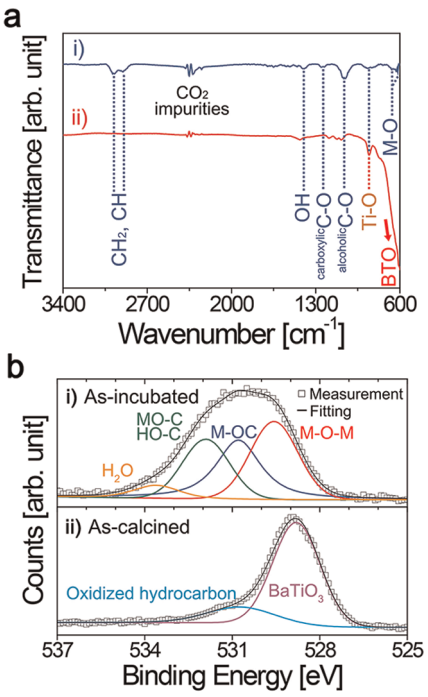

Figure 2. Chemical characterization of virus-metal ions complex and virus-templated BTO. ATR-IR spectroscopy and O1s XPS analysis measured before and after calcination. (a) There are bands suggestive of complexation at the as-incubated state, whereas only the BTO-specific spectrum is shown at the as-calcined state. (b) The deconvolution of the O1s envelope before the calcination process displays chelation between the virus-template and the metal-ions from glycolates. After calcination, the sharp BTO peak at low binding energy is emitted with a small hydrocarbon shoulder.

The intermediate compositions or phases during heat treatments in various BTO synthesis methods are highly important because of the large activation energy of BTO crystallization.[43] Thermogravimetry (TG) and differential scanning calorimetry (DSC) analyses show that the vaporization of water and the burning of M13 phage occur at 100—200 and 200—400 °C, respectively (Figure 3a). Although the carbon sources of glycolates are burned even after 400 °C (see TG), there is a broad endothermic region in the DSC due to the annealing and diffusion of the two metal elements. For calcination at 600—900 °C, the thermal treatment is insufficient, producing various titanium-rich compositions or phases, as observed by Raman spectroscopy (Figure S9).[50] The bands of Raman shift for final virus-templated BTO nanostructures correspond to the general result of tetragonal perovskite BTO (Figure 3b). In particular, only the tetragonal phase can show the B_1 and E modes at 307 cm^{-1} and the high-frequency longitudinal optic mode at 715 cm^{-1}, which are

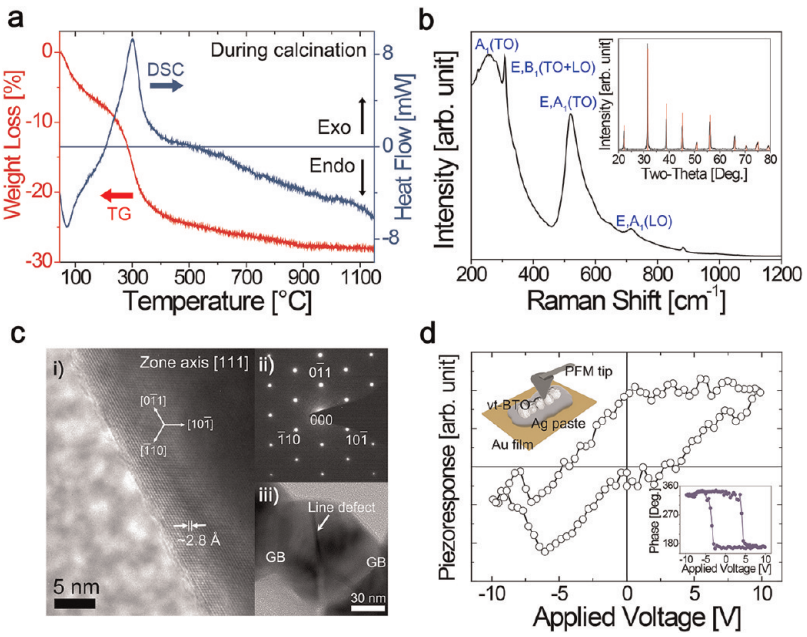

Figure 3. Thermal analysis during calcination and material characterization of virus template BTO. (a) TG and DSC analysis during calcination from 50 to 1150 °C with 0.1 °C·s^{-1}. (b) Raman scattering spectrum of the virus-templated BTO nanocrystals. The indexed bands are in agreement with the typical tetragonal phase of perovskite BTO. The inset presents XRD patterns of virus-templated BTO, corresponding to *P4mm* crystal symmetry (JCPDS# 005-0626). (c) (i and ii) HRTEM image and SAED patterns along the [111] zone-axis of the nanostructured BTO. (iii) GBs and one-dimensional defect are indicated in the TEM micrograph. (d) Remanent piezoresponse hysteresis property as a function of DC voltage bias. The inset hysteresis curve shows the inversion of the piezoelectric phase (dipole switching). Virus-templated BTO is denoted as 'vt-BTO'.

experimental evidence of the cubic-to-tetragonal phase transformation.[51] The XRD patterns also define the P3 mm crystalline structure of BTO (inset of Figure 3b). The perfect crystallinity of virus-templated BTO is presented by the HRTEM and SAED along the [111] zone-axis, showing near 3-fold symmetry (Figure 3c-i,c-ii). The existing grain boundaries (GBs) and large growth dislocation,[52] as indicated in Figure 3c-iii, confirm that the synthesized virus-templated BTO nanostructures are derived from the virus-metal ionic complex, not from just the agglomeration of BTO particles. Piezoresponse hysteresis measurement is performed to identify the switching behavior of polarization in the resultant virus-templated BTO domains (Figure 3d). This remanent hysteresis loop is the result of detecting piezoresponse after turning off the electric field. The phase hysteresis displays perfectly switchable dipoles (inset of Figure 3d), so the retention properties of the piezoelectricity are revealed despite a slight deviation of piezoresponse caused by the mechanical instability of a silver paste electrode.

To harvest energy using the piezoelectric virus-templated BTO, a well-established nanogenerator fabrication process is utilized,[3] as illustrated by the schematics of Figure 4a. The stirred and infiltrated virus-templated BTO nanostructures are mixed with polydimethylsiloxane (PDMS) to achieve the BTO piezoelectric layer (Figure 4a-i). The indium tin oxide (ITO)-coated thick (~175 μm) polyethylene terephthalate (PET) substrate is covered with PDMS dielectric layer to prevent the electric breakdown of device (Figure 4a-ii). Next, the virus-templated BTO-based piezoelectric layer (~200 μm in thickness, Figure S10) was spin-casted on a PDMS-coated flexible substrate. For the top electrode, an ITO-deposited thin PET substrate (~50 μm) is subsequently placed on the piezoelectric layer (Figure 4a-iii). Figure 4a-iv shows the photograph of fabricated virus-templated BTO nanogenerator, which is malleable and flexible. It is theoretically and experimentally well-established that percolated nanostructures of one-dimensional fibrous materials can be well distributed in three-dimensional active regions.[29,30,53−55] Figure S11 also shows a well-dispersed, virus-templated BTO piezo-layer that originated from the percolation of one-dimensional nanostructures, whereas BTO NPs are significantly aggregated in the PDMS matrix.[3,15,40] Due to the anisotropic structure of M13, the well-percolated nanoclusters of the virus-templated BTO were well-distributed in a soft elastomeric matrix without any dispersion agents, as shown in the high resolution scanning electron microscope (SEM) image of Figure 4a-v.

Figure 4b shows the output performance of the virus-templated BTO nanogenerator by periodical bending/releasing motion. The short-circuit current and open-circuit voltage measured from the nanogenerator device with an effective area of 2.5 × 2.5 cm^2 reach up to ~300 nA and ~6 V, respectively, which correspond to the previously reported theoretical study.[40] In addition, this virus-templated BTO nanogenerator exhibits high output compared to that

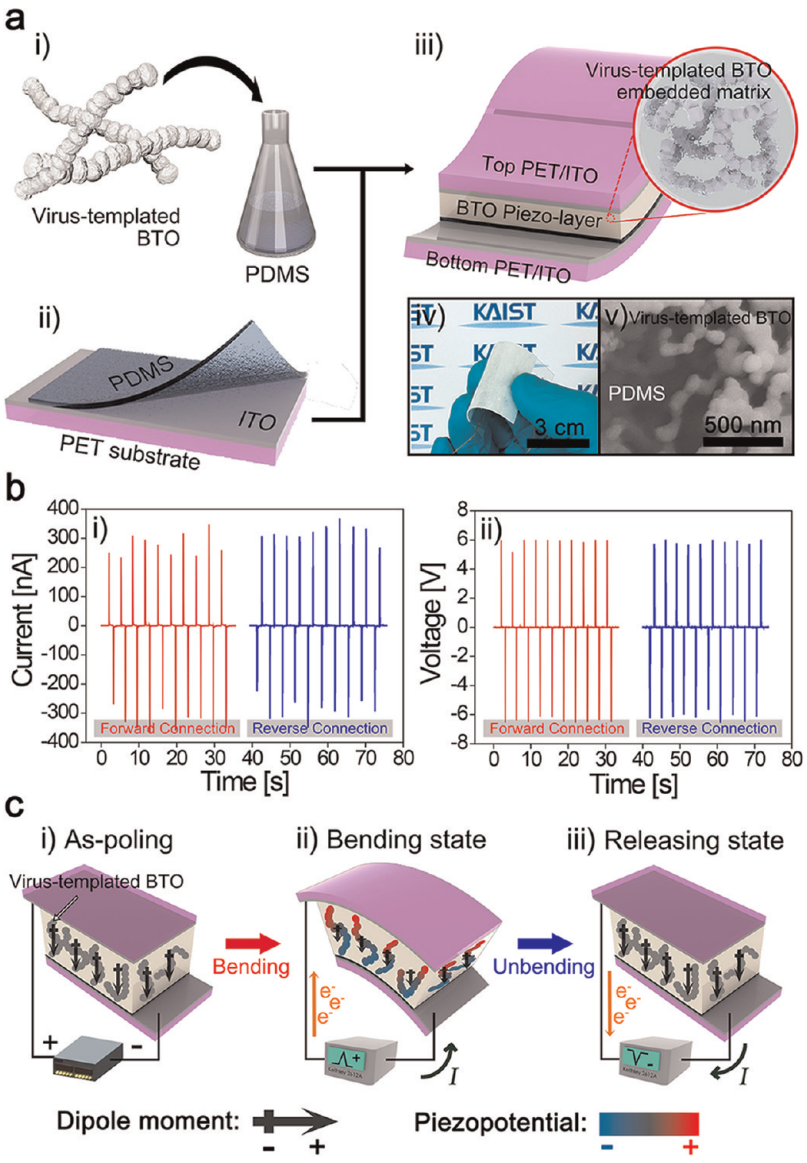

Figure 4. Nanogenerator fabrication and energy harvesting from mechanical deformation. (a) (i–iii) Schematics of the fabrication process for a nanogenerator device. (iv) Photograph of the final nanogenerator and (v) SEM micrograph of well-entangled BTO nanocrystal clusters in the PDMS matrix. (b) The measured (i) short-circuit current and (ii) open-circuit voltage signals of the virus-templated nanogenerator device in both forward and reverse connections with a curvature radius of 5 cm, frequency of 0.3 Hz, and rate of 0.2 m·s^{-1}. The inversion of signals (switching polarity) indicates that the generated outputs are the genuine results from the nanogenerator. (c) The mechanism of energy harvesting from the nanogenerator device. (i) Dipole moments of the virus-templated BTO are definitely aligned in the direction of external electric field during the poling process. (ii) Built-in potential and current (electrons flow) are generated by the mechanical bending due to the produced piezoelectric potential. (iii) Since the piezopotential disappears when the stress is released, the accumulated charges flow back to the original state.

reported in other works, as summarized in Table S1. To confirm that the electrical signals are produced by the nanogenerator, the output current and voltage were measured under both forward and reverse connections with measurement equipment. The polarity of electrical signals in forward connection was inverted when the connection is reversely switched, as shown in Figure 4b-i,b-ii. These electrical outputs are higher than the results of our previously reported nanocomposite generator using BTO NPs with carbon nanotubes (CNTs) as dispersion improvers. This enhanced performance may be caused by the inherently dispersed structure of the virus-templated nanocrystals, while there is only physical mixing in the previous nanocomposite fabrication.

Figure 4c depicts the mechanism of energy conversion by the nanogenerator device. During the poling process (see Methods), the direction of electrical dipoles in the virus-templated BTO piezoelectric domain can be aligned along the external electrical field in parallel (Figure 4c-i). When the nanogenerator suffers from the mechanical deformation, the piezoelectric potential is induced between the top and bottom electrodes owing to the stress of dipoles (Figure 4c-ii).

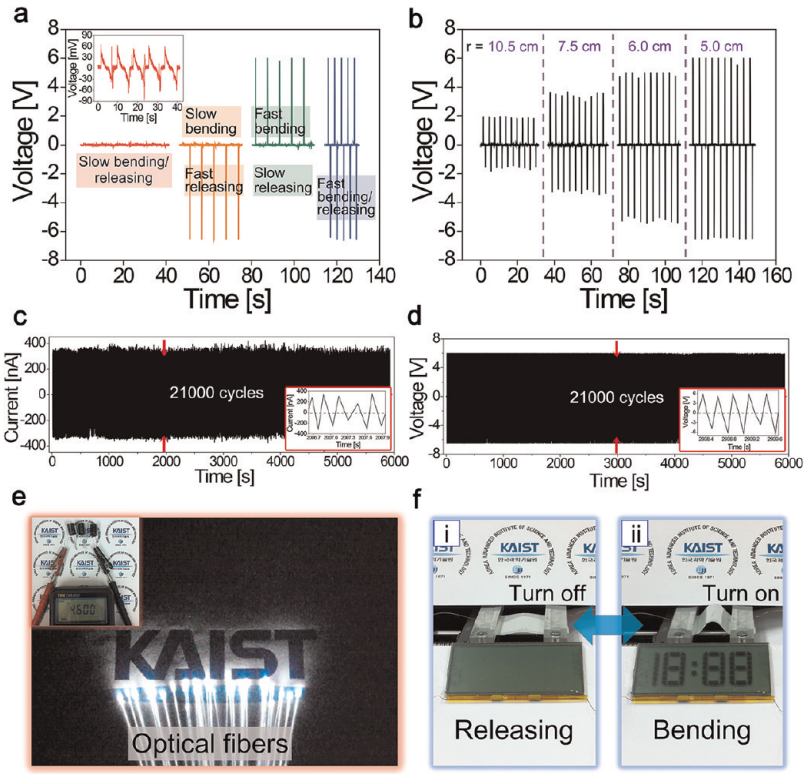

Figure 5. Characteristics and application of the virus-templated BTO nanogenerator device. Output voltage signals generated by the virus-templated nanogenerator device according to (a) strain rate (0.2 *vs* 0.005 m·s^{-1}) and (b) radius of curvature (r = 5.0−10.5 cm). A larger radius of curvature means a smaller degree of strain. (c and d) Stable energy generation test performed to confirm the mechanical durability of the virus-templated BTO based nanogenerator device. (e) Captured photograph of the moment of lighting up the white LED-based optical fibers using the electrical energy stored by the virus-templated BTO-nanogenerator. The inset shows the three capacitors in series charged by mechanical deformation of the nanogenerator for 4 h (charged voltage is about 4.6 V). (f) Commercial LCD driven by electric power from bending and releasing motions of the virus-templated BTO nanogenerator. Logo use permitted by Copyright 2013 KAIST.

The formed built-in potential results in the flow of free electrons which neutralizes the electric field produced by the dipoles. Since the virus-templated BTO piezoelectric layer and the dielectric PDMS are insulators, the current only flows through external circuitry, so there is no charge leakage throughout the periodical measurement. At a static strain, the built-in potential is faded out because the piezopotential is balanced by the accumulated free charges at both electrodes. When the strain disappears, the piezoelectric potential vanishes and an opposite built-in potential is formed by the free charges accumulated at both ends of the external circuit (Figure 4c-iii). The free electrons flow back in the opposite direction, and subsequently the current diminishes to zero.

The output performance of virus-templated BTO nanogenerator is affected by the strain rate, as the piezoelectric bound charges are constant at the same degree of strain. For the constant strain, the faster strain rate results in a higher output voltage (Figure 5a). Likewise, the outputs also increase with the bending curvature at the given strain rate (Figure 5b) since a more deformed piezoelectric layer can produce a larger built-in potential along the circuit. The stability of the virus-templated BTO based nanogenerator is estimated through measurement over extended cycling times (∼21000 cycles) at fast frequency. Figure 5c,d shows that the output signals are relatively stable with no significant degradation of performance during the durability test. The generated current and voltage of the nanogenerator device under fast frequency (3.5 Hz) were almost the same as the measurement under the original frequency. These results demonstrate that the nanogenerator fabricated by virus-templated BTO nanostructure is highly stable and suitable for energy harvesting from irregular agitations (insets of Figure 5c,d). The slight deviation of signals may be attributed to the shortage in the response time of the measurement unit caused by the harsh mechanical conditions. Also, the generated electrical energy can be used to operate commercial devices without an external energy source. Three 1 mF capacitors connected in parallel were charged by bending/releasing motions of the virus-templated BTO nanogenerator device with bridge rectifier circuitry (Figure S15). The stored voltage of each capacitor under the external mechanical deformation reaches up to about 1.5 V generated from the nanogenerator device (the total stored voltage is about 4.6 V). Finally, the white light emitting diode (LED)-based optical fibers are successfully driven (Figure 5e and Video S1).

Moreover, the LCD was fully operated by the repeated positive/negative electrical signals from the virus-templated BTO based nanogenerator (Figure 5f). The alternating signals can turn on the LCD device with no rectifier, as an LCD is a nonpolar device. Supporting Information Video S2 presents the LCD screen driven by bending/releasing motions of the nanogenerator device with frequencies of 0.3 and 5 Hz.

CONCLUSION

In this study, we have developed a biological self-assembly method for dispersed and high crystalline perovskite material using a genetically modified virus to fabricate the self-powered flexible energy harvesting device. The virus-templated BTO nanostructure originated from the virus-metal ionic complex based on the crucial interactions between metal-based ligands and genetic engineered proteins. The complexation and calcination events are characterized to investigate their chemical states and materials properties. Excellent output performance (~300 nA and ~6 V) is successfully obtained from the virus-templated BTO nanogenerator by periodical mechanical motions. The commercial electrical devices are driven by the harvested energy from the virus-templated BTO nanogenerator. We expect that the charge effect of ligands and chelating effect of glutamates studied in our research can help to understand the versatility of biotemplate synthesis. Furthermore, we believe that our biosynthetic route for inorganic nanostructures can open a new era of bioinspired self-assembly technology, such as biomechanical energy harvesting, thermoelectric applications, and biofuel cells.

METHODS

Virus-Templated BTO Synthesis. $BaCl_2 \cdot 2H_2O$ (Sigma-Aldrich) and $TiCl_4$ (Sigma-Aldrich) were dissolved into ethylene glycol (Sigma-Aldrich) with magnetic stirring overnight to make barium and titanium glycolate solutions, respectively. The E3-M13 virus solution was prepared as a concentration of 10^{13} pfu·mL^{-1} suspended in TBS (pH 7.5).

First, 0.1 mL of the barium glycolate solution was mixed with 20 mL of the virus solution, and then 5 M NaOH (Sigma-Aldrich) solution was slowly added to adjust pH to 10. The virus solution was incubated with the barium precursor with magnetic stirring at 200 rpm for 2 h. Next, 0.1 mL of the titanium glycolate solution was added to the barium glycolate preincubated virus solution. The total solution was maintained at 80 °C overnight to form a virus-metal ionic complex. The obtained virus-metal ionic complex was purified by centrifugation (RFC 11000*g*) and washing with deionized water (DI water, Milli-Q, Millipore) three times. The freeze-drying process was performed to evaporate water from the purified complex. After calcination of the virus-metal ionic complex at 1000 °C for 1−2 h in ambient air condition, virus-templated high-crystalline BTO was formed.

Nanogenerator Fabrication. The synthesized virus-templated BTO nanocrystals were mixed with a PDMS elastomer (Sylgard 184, Dow Corning) matrix for the piezoelectric layer (1:5 w/w ratio of BTO to PDMS). Then, this piezoelectric layer was spin-casted onto a PDMS/ITO (100 nm)/PET (175 μm, Sigma-Aldrich) flexible substrate at a rate of 1500 rpm for 40 s and cured at 75 °C for 5 min. Next, another ITO-deposited PET film (50 μm, SKC) was placed on a bottom piezoelectric layer/PDMS/ITO/PET substrate and fully hardened at 75 °C for 24 h. Copper cables were connected to ITO electrodes by using conductive epoxy (Chemtronics) to measure the output current and voltage signals. Finally, to enhance the piezoelectric effect of device, the virus-templated BTO nanogenerator device was poled at 130 °C with a direct current (DC) voltage of 2 kV for 12 h.

Conflict of Interest: The authors declare no competing financial interest.

Supporting Information Available: Texts explaining detailed virus-engineering steps, analyses equipment, and calculation for yield of synthesis. Figures and texts of an additional COMSOL-FEA simulation, TEM images and Raman spectra of various synthesis conditions, SAED and XRD patterns before calcination, issue of bundling and aggregation, a low-magnified TEM micrograph for showing well-dispersed virus-templated BTO, XPS data of bare E3-M13 bacteriophage, generated electrical outputs from the virus-templated BTO nanogenerator poled with various external fields, generated outputs from the only BTO NPs composite-based nanogenerator, and the rectified voltage of virus-templated BTO nanogenerator. A table providing a comparison of this study with previously reported nanogenerators. Videos showing operated LED-based optical fibers and LCD screen by generated electrical energy from the virus-templated BTO nanogenerator. This material is available free of charge *via* the Internet at http://pubs.acs.org.

Acknowledgment. C. K. Jeong and I. Kim contributed equally to this work. This work was financially supported by the Basic Science Research Program (NRF-2012R1A2A1A03010415) funded by the Korea government (MSIP) through the National Research Foundation of Korea (NRF), and the Center for Integrated Smart Sensors funded by the Ministry of Science, ICT & Future Planning as Global Frontier Project (CISS-2012M3A6A6054187). Also, this work was supported under the framework of international cooperation program managed by National Research Foundation of Korea (NRF-2012K2A1A2033167) and by Basic Science Research Program through the National Research Foundation of Korea (NRF) funded by the Ministry of Science, ICT & Future Planning (NRF-2013R1A1A1009626).

REFERENCES AND NOTES

1. Aubrecht, G. J. *Energy: Physical, Environmental, and Social Impact*; Pearson Prentice Hall: Upper Saddle River, NJ, 2006.
2. Priya, S.; Inman, D. J. *Energy Harvesting Technologies*; Springer: New York, 2009.
3. Park, K. I.; Lee, M.; Liu, Y.; Moon, S.; Hwang, G. T.; Zhu, G.; Kim, J. E.; Kim, S. O.; Kim, D. K.; Wang, Z. L.; *et al.* Flexible Nanocomposite Generator Made of $BaTiO_3$ Nanoparticles and Graphitic Carbons. *Adv. Mater.* **2012**, *24*, 2999–3004.
4. Beeby, S. P.; Tudor, M. J.; White, N. M. Energy Harvesting Vibration Sources for Microsystems Applications. *Meas. Sci. Technol.* **2006**, *17*, R175–R195.
5. Wang, Z. L. *Nanogenerators for Self-Powered Devices and Systems*; Georgia Institue of Technology: Atlanta, GA, 2011.
6. Qi, Y.; McAlpine, M. C. Nanotechnology-Enabled Flexible and Biocompatible Energy Harvesting. *Energy Environ. Sci.* **2010**, *3*, 1275–1285.
7. Wang, Z. L.; Song, J. H. Piezoelectric Nanogenerators Based on Zinc Oxide Nanowire Arrays. *Science* **2006**, *312*, 242–246.
8. Qin, Y.; Wang, X. D.; Wang, Z. L. Microfibre-Nanowire Hybrid Structure for Energy Scavenging. *Nature* **2008**, *451*, 809–813.
9. Yang, R. S.; Qin, Y.; Dai, L. M.; Wang, Z. L. Power Generation with Laterally Packaged Piezoelectric Fine Wires. *Nat. Nanotechnol.* **2009**, *4*, 34–39.
10. Xu, S.; Qin, Y.; Xu, C.; Wei, Y. G.; Yang, R. S.; Wang, Z. L. Self-Powered Nanowire Devices. *Nat. Nanotechnol.* **2010**, *5*, 366–373.
11. Persano, L.; Dagdeviren, C.; Su, Y.; Zhang, Y.; Girardo, S.; Pisignano, D.; Huang, Y.; Rogers, J. A. High Performance

Piezoelectric Devices Based on Aligned Arrays of Nanofibers of Poly(vinylidenefluoride-co-trifluoroethylene). *Nat. Commun.* **2013**, *4*, 1633.
12. Chung, S. Y.; Kim, S.; Lee, J. H.; Kim, K.; Kim, S. W.; Kang, C. Y.; Yoon, S. J.; Kim, Y. S. All-Solution-Processed Flexible Thin Film Piezoelectric Nanogenerator. *Adv. Mater.* **2012**, *24*, 6022–6027.
13. Gu, L.; Cui, N. Y.; Cheng, L.; Xu, Q.; Bai, S.; Yuan, M. M.; Wu, W. W.; Liu, J. M.; Zhao, Y.; Ma, F.; *et al.* Flexible Fiber Nanogenerator with 209 V Output Voltage Directly Powers a Light-Emitting Diode. *Nano Lett.* **2013**, *13*, 91–94.
14. Qi, Y.; Kim, J.; Nguyen, T. D.; Lisko, B.; Purohit, P. K.; McAlpine, M. C. Enhanced Piezoelectricity and Stretchability in Energy Harvesting Devices Fabricated from Buckled PZT Ribbons. *Nano Lett.* **2011**, *11*, 1331–1336.
15. Park, K. I.; Jeong, C. K.; Ryu, J.; Hwang, G. T.; Lee, K. J. Flexible and Large-Area Nanocomposite Generator Based on Lead Zirconate Titanate Particles and Carbon Nanotubes. *Adv. Energy Mater.* **2013**, 10.1002/aenm.201300458.
16. Park, K. I.; Xu, S.; Liu, Y.; Hwang, G. T.; Kang, S. J. L.; Wang, Z. L.; Lee, K. J. Piezoelectric $BaTiO_3$ Thin Film Nanogenerator on Plastic Substrates. *Nano Lett.* **2010**, *10*, 4939–4943.
17. Park, J. B.; Kelly, B. J.; Kenner, G. H.; Vonrecum, A. F.; Grether, M. F.; Coffeen, W. W. Piezoelectric Ceramic Implants - *Invivo* Results. *J. Biomed. Mater. Res.* **1981**, *15*, 103–110.
18. Um, M. H.; Kumazawa, H. Hydrothermal Synthesis of Ferroelectric Barium and Strontium Titanate Extremely Fine Particles. *J. Mater. Sci.* **2000**, *35*, 1295–1300.
19. O'Brien, S.; Brus, L.; Murray, C. B. Synthesis of Monodisperse Nanoparticles of Barium Titanate: Toward a Generalized Strategy of Oxide Nanoparticle Synthesis. *J. Am. Chem. Soc.* **2001**, *123*, 12085–12086.
20. Nuraje, N.; Dang, X. N.; Qi, J. F.; Allen, M. A.; Lei, Y.; Belcher, A. M. Biotemplated Synthesis of Perovskite Nanomaterials for Solar Energy Conversion. *Adv. Mater.* **2012**, *24*, 2885–2889.
21. Sarikaya, M.; Tamerler, C.; Jen, A. K. Y.; Schulten, K.; Baneyx, F. Molecular Biomimetics: Nanotechnology through Biology. *Nat. Mater.* **2003**, *2*, 577–585.
22. Kim, S.; Park, C. B. Bio-Inspired Synthesis of Minerals for Energy, Environment, and Medicinal Applications. *Adv. Funct. Mater.* **2013**, *23*, 10–25.
23. Yan, H.; Park, S. H.; Finkelstein, G.; Reif, J. H.; LaBean, T. H. DNA-Templated Self-Assembly of Protein Arrays and Highly Conductive Nanowires. *Science* **2003**, *301*, 1882–1884.
24. Mao, C. B.; Solis, D. J.; Reiss, B. D.; Kottmann, S. T.; Sweeney, R. Y.; Hayhurst, A.; Georgiou, G.; Iverson, B.; Belcher, A. M. Virus-Based Toolkit for the Directed Synthesis of Magnetic and Semiconducting Nanowires. *Science* **2004**, *303*, 213–217.
25. Lee, S. W.; Mao, C. B.; Flynn, C. E.; Belcher, A. M. Ordering of Quantum Dots Using Genetically Engineered Viruses. *Science* **2002**, *296*, 892–895.
26. Malvankar, N. S.; Vargas, M.; Nevin, K. P.; Franks, A. E.; Leang, C.; Kim, B. C.; Inoue, K.; Mester, T.; Covalla, S. F.; Johnson, J. P.; *et al.* Tunable Metallic-Like Conductivity in Microbial Nanowire Networks. *Nat. Nanotechnol.* **2011**, *6*, 573–579.
27. Belcher, A. M.; Wu, X. H.; Christensen, R. J.; Hansma, P. K.; Stucky, G. D.; Morse, D. E. Control of Crystal Phase Switching and Orientation by Soluble Mollusc-Shell Proteins. *Nature* **1996**, *381*, 56–58.
28. Naik, R. R.; Stringer, S. J.; Agarwal, G.; Jones, S. E.; Stone, M. O. Biomimetic Synthesis and Patterning of Silver Nanoparticles. *Nat. Mater.* **2002**, *1*, 169–172.
29. Lee, Y. J.; Yi, H.; Kim, W. J.; Kang, K.; Yun, D. S.; Strano, M. S.; Ceder, G.; Belcher, A. M. Fabricating Genetically Engineered High-Power Lithium-Ion Batteries Using Multiple Virus Genes. *Science* **2009**, *324*, 1051–1055.
30. Lee, Y.; Kim, J.; Yun, D. S.; Nam, Y. S.; Shao-Horn, Y.; Belcher, A. M. Virus-Templated Au and Au-Pt Core-Shell Nanowires and Their Electrocatalytic Activities for Fuel Cell Applications. *Energy Environ. Sci.* **2012**, *5*, 8328–8334.
31. Dang, X. N.; Yi, H. J.; Ham, M. H.; Qi, J. F.; Yun, D. S.; Ladewski, R.; Strano, M. S.; Hammond, P. T.; Belcher, A. M. Virus-Templated Self-Assembled Single-Walled Carbon Nanotubes for Highly Efficient Electron Collection in Photovoltaic Devices. *Nat. Nanotechnol.* **2011**, *6*, 377–384.
32. Nam, Y. S.; Magyar, A. P.; Lee, D.; Kim, J. W.; Yun, D. S.; Park, H.; Pollom, T. S.; Weitz, D. A.; Belcher, A. M. Biologically Templated Photocatalytic Nanostructures for Sustained Light-Driven Water Oxidation. *Nat. Nanotechnol.* **2010**, *5*, 340–344.
33. Nam, Y. S.; Shin, T.; Park, H.; Magyar, A. P.; Choi, K.; Fantner, G.; Nelson, K. A.; Belcher, A. M. Virus-Templated Assembly of Porphyrins into Light-Harvesting Nanoantennae. *J. Am. Chem. Soc.* **2010**, *132*, 1462–1463.
34. Ghosh, D.; Lee, Y.; Thomas, S.; Kohli, A. G.; Yun, D. S.; Belcher, A. M.; Kelly, K. A. M13-Templated Magnetic Nanoparticles for Targeted *in Vivo* Imaging of Prostate Cancer. *Nat. Nanotechnol.* **2012**, *7*, 677–682.
35. Tseng, R. J.; Tsai, C. L.; Ma, L. P.; Ouyang, J. Y. Digital Memory Device Based on Tobacco Mosaic Virus Conjugated with Nanoparticles. *Nat. Nanotechnol.* **2006**, *1*, 72–77.
36. Nam, Y. S.; Park, H.; Magyar, A. P.; Yun, D. S.; Pollom, T. S.; Belcher, A. M. Virus-Templated Iridium Oxide-Gold Hybrid Nanowires for Electrochromic Application. *Nanoscale* **2012**, *4*, 3405–3409.
37. Pokorski, J. K.; Steinmetz, N. F. The Art of Engineering Viral Nanoparticles. *Mol. Pharmaceutics* **2011**, *8*, 29–43.
38. Nam, K. T.; Kim, D. W.; Yoo, P. J.; Chiang, C. Y.; Meethong, N.; Hammond, P. T.; Chiang, Y. M.; Belcher, A. M. Virus-Enabled Synthesis and Assembly of Nanowires for Lithium Ion Battery Electrodes. *Science* **2006**, *312*, 885–888.
39. Lee, B. Y.; Zhang, J. X.; Zueger, C.; Chung, W. J.; Yoo, S. Y.; Wang, E.; Meyer, J.; Ramesh, R.; Lee, S. W. Virus-Based Piezoelectric Energy Generation. *Nat. Nanotechnol.* **2012**, *7*, 351–356.
40. Lin, Z. H.; Yang, Y.; Wu, J. M.; Liu, Y.; Zhang, F.; Wang, Z. L. $BaTiO_3$ Nanotubes-Based Flexible and Transparent Nanogenerators. *J. Phys. Chem. Lett.* **2012**, *3*, 3599–3604.
41. Day, V. W.; Eberspacher, T. A.; Frey, M. H.; Klemperer, W. G.; Liang, S.; Payne, D. A. Barium Titanium Glycolate: A New Barium Titanate Powder Precursor. *Chem. Mater.* **1996**, *8*, 330–332.
42. Day, V. W.; Eberspacher, T. A.; Klemperer, W. G.; Liang, S. Barium Titanium Alkoxides for Barium Titanates: Synthesis, Characterization, and Applications. *Mater. Res. Soc. Symp. Proc.* **1994**, *335*, 177–182.
43. Walton, R. I.; Millange, F.; Smith, R. I.; Hansen, T. C.; O'Hare, D. Real Time Observation of the Hydrothermal Crystallization of Barium Titanate Using *in Situ* Neutron Powder Diffraction. *J. Am. Chem. Soc.* **2001**, *123*, 12547–12555.
44. Zhao, Z.; Buscaglia, V.; Viviani, M.; Buscaglia, M. T.; Mitoseriu, L.; Testino, A.; Nygren, M.; Johnsson, M.; Nanni, P. Grain-Size Effects on the Ferroelectric Behavior of Dense Nanocrystalline $BaTiO_3$ Ceramics. *Phys. Rev. B* **2004**, *70*, 024107.
45. Han, J. J.; Zhang, H.; Li, Y. Z.; Zhao, X. J.; Chen, H.; Wu, Z. K.; Kim, S. J.; Park, K. S. Fabrication of TiO_2 Microrod with Desired Shapes from Rod-like Titanium Glycolate. *Chem. Lett.* **2007**, *36*, 1352–1353.
46. Yu, P. F.; Cui, B.; Shi, Q. Z. Preparation and Characterization of $BaTiO_3$ Powders and Ceramics by Sol-Gel Process Using Oleic Acid as Surfactant. *Mater. Sci. Eng., A* **2008**, *473*, 34–41.
47. Huang, C. J.; Lin, J. J.; Shieu, F. S. Formation Mechanism and Characterization of Ag-Metal Chelate Polymer Prepared by a Wet Chemical Process. *Jpn. J. Appl. Phys.* **2005**, *44*, 6332–6340.
48. Polzonetti, G.; Battocchio, C.; Dettin, M.; Gambaretto, R.; Di Bello, C.; Carravetta, V.; Monti, S.; Iucci, G. Self-Assembling Peptides: A Combined XPS and NEXAFS Investigation on the Structure of Two Dipeptides Ala-Glu, Ala-Lys. *Mater. Sci. Eng. C* **2008**, *28*, 309–315.
49. Wegmann, M.; Watson, L.; Hendry, A. XPS Analysis of Submicrometer Barium Titanate Powder. *J. Am. Ceram. Soc.* **2004**, *87*, 371–377.
50. Rossel, M.; Hohe, H. R.; Leipner, H. S.; Voltzke, D.; Abicht, H. P.; Hollricher, O.; Muller, J.; Gablenz, S. Raman Microscopic Investigations of $BaTiO_3$ Precursors with Core-Shell Structure. *Anal. Bioanal. Chem.* **2004**, *380*, 157–162.
51. Li, A. D.; Ge, C. Z.; Lu, P.; Wu, D.; Xiong, S. B.; Ming, N. B. Fabrication and Electrical Properties of Sol-Gel Derived $BaTiO_3$ Films with Metallic $LaNiO_3$ Electrode. *Appl. Phys. Lett.* **1997**, *70*, 1616–1618.

52. Yang, Y. D.; Priya, S.; Li, J. F.; Viehland, D. Two-Phase Coexistence in Single-Grain $BaTiO_3$-$(Mn_{0.5}Zn_{0.5})Fe_2O_4$ Composites, *via* Solid-State Reaction. *J. Am. Ceram. Soc.* **2009**, *92*, 1552–1555.
53. Cheng, X.; Sastry, A. M.; Layton, B. E. Transport in Stochastic Fibrous Networks. *J. Eng. Mater. Technol.* **2001**, *123*, 12–19.
54. Berhan, L.; Sastry, A. M. On Modeling Bonds in Fused, Porous Networks: 3D Simulations of Fibrous-Particulate Joints. *J. Compos. Mater.* **2003**, *37*, 715–740.
55. Berhan, L.; Sastry, A. M. Modeling Percolation in High-Aspect-Ratio Fiber Systems. I. Soft-Core *versus* Hard-Core Models. *Phys. Rev. E* **2007**, *75*, 041120.